ADVANCED FUNCTIONAL MATERIALS
www.afm-journal.de

Nonequilibrium Thermal Shock Enabled Trapping of Metastable Multi-Element Alloy Anode for Potassium-Ion Batteries

Shuming Dou, Yueyue Shao, Longlong Fan, Danfeng Zhang, Jie Xu, Jingchao Zhang, Huijie Tian, Yan-Bing He, Chong Mao, He Zhu, Wei Gan, Jianrong Zeng, Wei-Di Liu, Jia Zhou,* Yanan Chen,* and Qunhui Yuan**

Metastable multi-element nanoalloys hold extensive potential for next-generation batteries due to their distinct structures. However, it is difficult to obtain metastable nanoalloys through conventional equilibrium annealing. Herein, the rapid nanomanufacturing of metastable multi-metallic nanoalloys is reported with single-phase structure, ultrafine size distribution, and high-density dispersion, realized by a novel nonequilibrium thermal shock (NTS) method. The NTS method, which features ultrafast heating/cooling rates and ultrashort treatment duration, can lead to the uniform mixing of different elements and the capture of the metastable state of multi-element nanoalloys while preventing interparticle sintering/coarsening and phase separation. As a proof-of-concept demonstration, a metastable BiSnSb nanoalloy (M-BiSnSb), prepared by the NTS method, exhibits rich lattice distortions and superior performance for potassium ion batteries (KIBs) compared with the stable BiSnSb (S-BiSnSb) anode prepared by a typical equilibrium method. Additionally, in situ high-temperature synchrotron X-ray diffraction (SXRD) demonstrates the formation mechanism of M-BiSnSb. Furthermore, in situ laboratory X-ray diffraction (XRD) and molecular dynamics (MD) simulation systematically prove the alloying reaction mechanism and the structural advantages of the metastable nanoalloys in diffusion-accelerating effect, respectively. This nonequilibrium nanomanufacturing strategy is expected to enable the rational and controllable synthesis of metastable nanomaterials for extensive electrochemical energy applications.

1. Introduction

Rechargeable potassium-ion batteries (KIBs) are rising as important alternatives to lithium-ion batteries (LIBs) for electric vehicles and large-scale grid storage systems, due to the low cost of potassium resources.[1] It is essential to develop suitable electrode materials for achieving high-performance KIBs. Alloying-type materials and carbonaceous materials have recently attracted increasing attention due to their attractive electrochemical properties, which are utilized as anode materials in KIBs.[2–6] Nevertheless, the large size of K^+ ions results in sluggish kinetics and severe volume expansion of the electrode materials during the repeated potassiation/depotassiation processes, which negatively affect the cycling performance.[7] Therefore, the development of innovative anode materials with high structural stability and electrochemical properties is imperative for K-ion storage devices.

Metastable nanomaterials are even more unique in terms of the physical structure and chemical properties that differ from the equilibrium state,[8,9] which has

S. Dou, H. Tian, Q. Yuan
Shenzhen Key Laboratory of Flexible Printed Electronics Technology and School of Materials Science and Engineering
Harbin Institute of Technology (Shenzhen)
Shenzhen 518055, China
E-mail: yuanqunhui@hit.edu.cn

S. Dou, J. Xu, J. Zhang, Y. Chen
School of Materials Science and Engineering
Key Laboratory of Advanced Ceramics and Machining Technology of Ministry of Education
Tianjin Key Laboratory of Composite and Functional Materials
Tianjin University
Tianjin 300072, China
E-mail: yananchen@tju.edu.cn

The ORCID identification number(s) for the author(s) of this article can be found under https://doi.org/10.1002/adfm.202412551

DOI: 10.1002/adfm.202412551

Y. Shao, W. Gan, J. Zhou
School of Science
Harbin Institute of Technology (Shenzhen)
Shenzhen 518055, China
E-mail: jiazhou@hit.edu.cn

L. Fan
Beijing Synchrotron Radiation Facility
Institute of High Energy Physics
Chinese Academy of Sciences
Beijing 100049, China

D. Zhang, Y.-B. He
Tsinghua Shenzhen International Graduate School
Tsinghua University
Shenzhen 518055, China

C. Mao
Zhuhai Smoothway Electronic Material Co., Ltd
Zhuhai 519050, China

attracted significant attention in energy storage systems. Furthermore, the distinctive features (e.g., defect/lattice distortion, amorphous configuration, medium/high-entropy structure, etc.) of metastable nanomaterials can provide the potential of attractive electrochemical performance in alkali metal-ion batteries. For example, the defective architecture in the graphite layers enables fast Li-ion diffusion kinetics by facilitating the phase transition.[10,11] The entropy stabilization effect of high-entropy oxides plays a critical role in improving the cycling stability of anode materials.[12,13] The open amorphous structure can offer abundant K-ion insertion sites for anode materials in KIBs.[14,15]

Recently, the controllable incorporation of multiple metallic elements into monophase alloy nanoparticles has raised new opportunities for electrode materials.[16,17] Multi-element alloy nanoparticles have increasing structural complexity and superior properties than single-element metal nanoparticles.[18,19] Therefore, the controllable incorporation of metastable structure into a multi-element nanoalloy is desirable to achieve the exciting and unexpected electrochemical properties of anode materials in KIBs, yet faces a great challenge using the traditional synthesis method. Furthermore, with the inherently slow heating/quenching rate (<1 K s^{-1}) and long sintering times (several hours), conventional alloy preparation typically results in uneven size distribution, element segregation, or phase separation, leading to a narrowed compositional space of multi-element nanoalloys.[20,21] Some efforts have been made to produce multi-element alloy nanoparticles by a carbothermal shock method,[22,23] where an ultra-high ramp rate (10^2–10^5 K s^{-1}) and a second-short shock duration allow the aforementioned disadvantages to be eliminated. However, this method usually relies on conductive free-standing carbon-based substrates (e.g., carbon nanofiber and carbonized wood).[20,22,24] This makes it difficult to meet the requirement of the large-scale production of nanomaterial powders, which limits their practical application in KIBs. Therefore, it is highly desired to develop a high-efficiency modified strategy for preparing high-quality metastable multi-element nanoalloy anodes with high potassium-storage performance, in which the new class of nanoalloys and performance enhancement mechanism should also be systematically explored.

Herein, we report a rapid nonequilibrium thermal shock (NTS) strategy for the synthesis of metastable multi-element alloy nanoparticles with single-phase structure, abundant lattice defects, homogeneous ultrafine-size distribution, and high-density dispersion for KIBs anodes (**Figure 1**). The nanomanufacturing process is carried out within ≈18 s due to the rapid heating/quenching rates (≈10^3 K min^{-1}). The transient high-temperature annealing converts alloy anchoring agents into N/O co-doped carbon nanosheets and creates favorable conditions for the uniform distribution of multi-element alloy nanoparticles. The nonequilibrium synthesis, featured by ultrafast cooling rate and ultrashort heating time, leads to the homogeneous mixing of different metal elements by facilitating kinetic control, effectively suppressing interparticle sintering/coarsening and phase separation, and trapping the metastable state of multi-element alloy nanoparticles during the phase transition process.[25] As a proof-of-concept demonstration, the defect-rich metastable medium entropy nanoalloy BiSnSb (M-BiSnSb), is synthesized and applied as an anode in KIBs, which exhibits better electrochemical performance than the stable medium entropy nanoalloy BiSnSb with fewer defects (S-BiSnSb, obtained by tube furnace calcination). In situ high-temperature synchrotron X-ray diffraction (SXRD) shows the structural evaluation of BiSnSb during the NTS process. Besides, in situ laboratory X-ray diffraction (XRD) reveals the potassiation/depotassiation reaction mechanism of BiSnSb. The molecular dynamics (MD) simulations are further employed to analyze the rapid channel diffusion behavior in the metastable BiSnSb system. This work expands an unlimited space for the synthesis of various high-quality and innovative metastable nanomaterials toward extensive electrochemical energy conversion and storage applications.

2. Results and Discussion

In situ characterization technique has been regarded as a powerful tool to provide transient and valuable information under operating conditions, which can help to investigate the formation/reaction mechanisms of advanced electrode materials.[26] The SXRD technique with a high-energy X-ray beam has advantages such as high sensitivity, high precision, and high efficiency.[27] Therefore, the in situ high-temperature SXRD technique excels in collecting convincing structural information of materials at an ultrafast speed, which is beneficial to observing the real-time phase transition and structure evolution of materials during the NTS preparation process. In this measurement, in situ high-temperature SXRD data is recorded every 2 s. **Figure 2A** presents a schematic diagram of in situ high-temperature SXRD measurement. The signal is obtained by the synchrotron X-ray source penetrating through the materials to the detector. The heating temperature and time can be precisely controlled by applying and removing the current pulse. Taking M-BiSnSb as an example, the structural evolution of precursor (metal salt and $C_6H_{17}N_3O_7$ coated on the surface of NaCl crystal particles) during the ultrashort duration of NTS is visualized in the contour plot of the in situ high-temperature SXRD results (Figure 2B). Figure 2C–F shows the morphological transition of the precursor at different NTS times using scanning electron microscopy (SEM). The NTS is characterized by nonequilibrium states, mainly due to the rapid heating and cooling in ultrashort durations. In a typical nonequilibrium synthesis process, the temperature was quickly raised to ≈770 K in 10 s and

H. Zhu
Herbert Gleiter Institute of Nanoscience
School of Materials Science and Engineering
Nanjing University of Science and Technology
Nanjing 210094, China

J. Zeng
Shanghai Synchrotron Radiation Facility
Shanghai Advanced Research Institute
Chinese Academy of Sciences
Shanghai 201204, China
E-mail: zengjr@sari.ac.cn

W.-D. Liu
School of Chemistry and Physics
ARC Research Hub in Zero-emission Power Generation for Carbon Neutrality
and Centre for Materials Science
Queensland University of Technology
Brisbane 4000, Australia

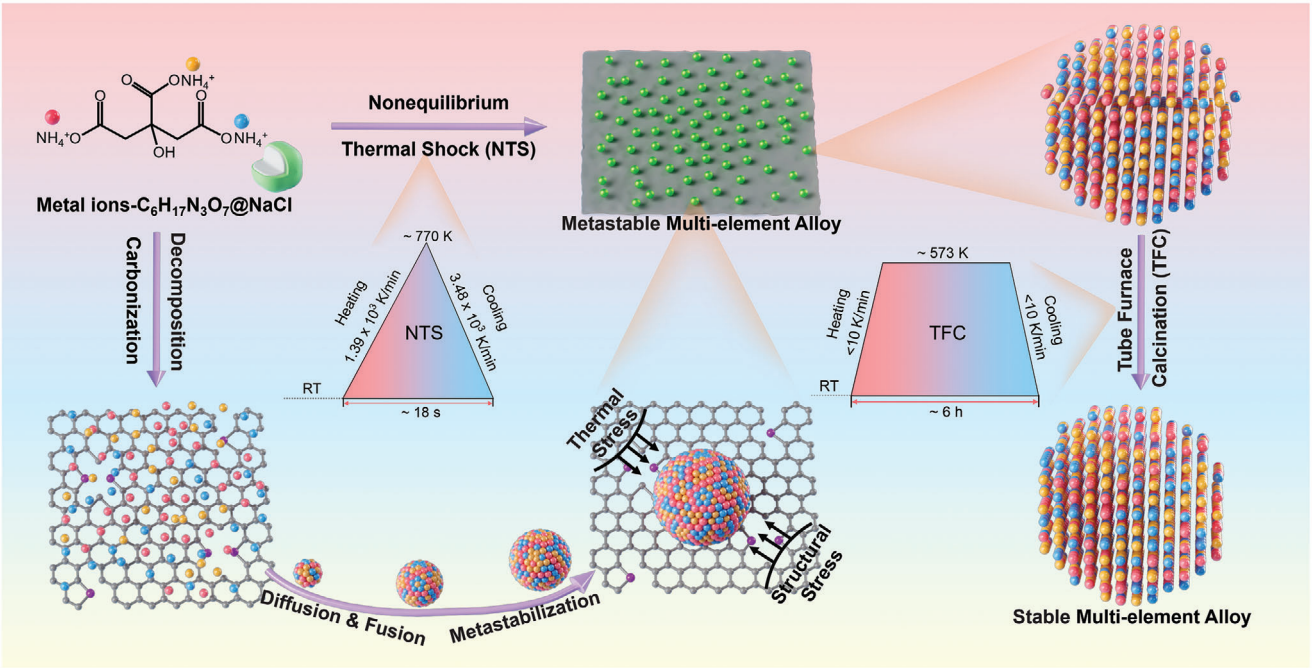

Figure 1. Schematic illustration of the nonequilibrium synthesis of metastable multi-element alloy nanoparticles. In contrast, the metastable multi-element alloy nanoparticles are stabilized via conventional equilibrium tube furnace calcination.

followed by rapid cooling to room temperature in 8 s. As shown in Figure 2C, before the NTS treatment, the smooth surface of the precursors is a layer of metal salt and $C_6H_{17}N_3O_7$. After applying an electric pulse, the intensity of the three peaks of precursor salts at 3.67°, 5.07°, and 5.30° gradually decreases and disappears (Figure 2B), demonstrating that the precursors are prone to decompose. In particular, the rapidly rising temperature enables the transformation of $C_6H_{17}N_3O_7$ into N/O-doped carbon sheets and the decomposition of metal salt into atoms/nanoclusters. Furthermore, the abundant defects in carbon sheets can provide numerous nucleation sites for the formation of nanoparticles.[28] With increasing the heating time during NTS, only the distorted

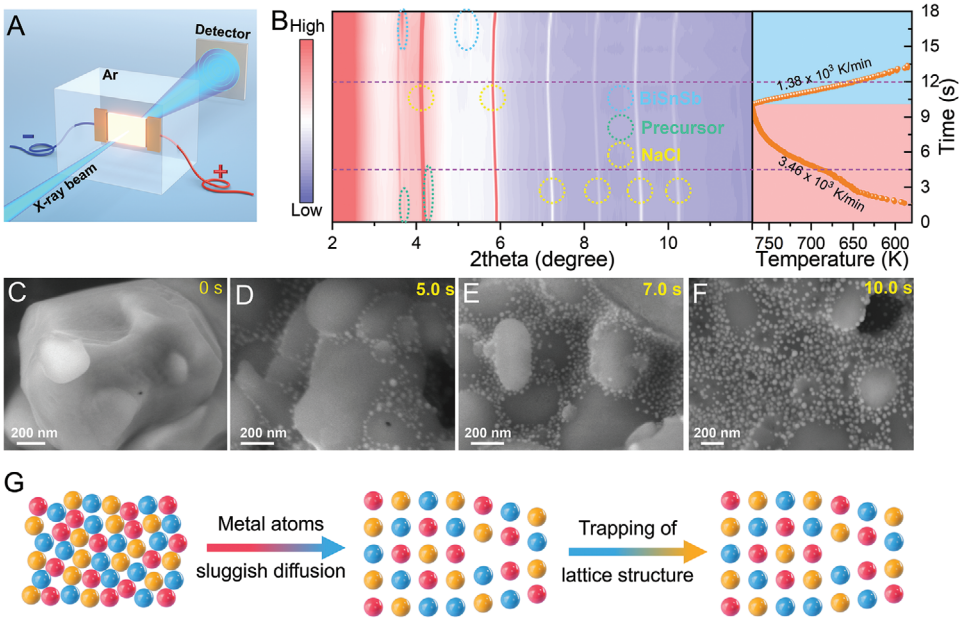

Figure 2. A) Schematic diagram of the NTS setup design for in situ high-temperature SXRD measurement. B) In situ high-temperature SXRD patterns and temporal evolution of temperature collected during the NTS process. C–F) SEM images of precursors under different NTS times. G) Schematic representation of the process by which metastable state is captured due to rapid quenching and nonequilibrium nanomanufacturing.

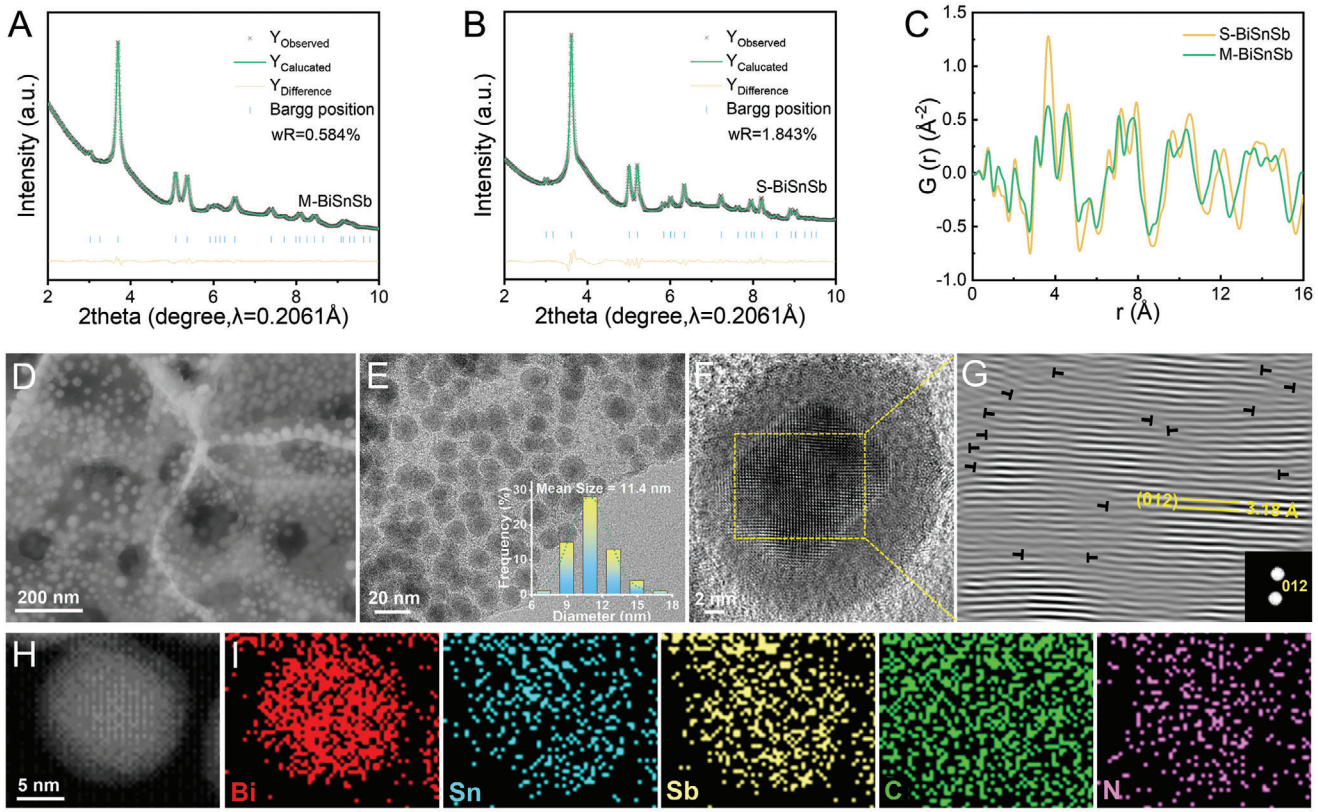

Figure 3. Rietveld refinement on SXRD patterns of A) M-BiSnSb and B) S-BiSnSb. C) Total PDF patterns of M-BiSnSb and S-BiSnSb. D) SEM image and E) high magnification TEM image of M-BiSnSb. Inset of Figure 3E: Nanoparticle size distribution of M-BiSnSb based on the high magnification TEM image. F) HRTEM image of M-BiSnSb. G) IFFT patterns of (012) plane from the region of the yellow box in Figure 3F. H) HAADF-STEM image and I) EDS elemental mapping images of M-BiSnSb.

diffraction peaks of NaCl can be observed, which is related to the thermal expansion of NaCl crystal particles. In addition to the nucleation process, the coalescence of the crystal nucleus and the homogenous mixing of the constituent metal elements happened simultaneously.

Interestingly, it is found that the characteristic peaks of M-BiSnSb appear during the rapid cooling process. The microstructural evolutions (Figure 2D–F), including the increase in nanoparticle size and surface coverage with extending heating time, correspond to the in situ high-temperature SXRD analysis. These results imply that the NTS synthesis can not only avoid the formation of bulk metal phases,[29] but also generate metastable multi-element nanoalloys.[25] Due to the confined diffusion of metal atoms with different metallic atomic radii in such a short time, some metal atoms are unable to reach their equilibrium positions and form steady-state alloy crystals, thus resulting in the formation of metastable multi-element nanoalloys characterized by abundant lattice distortions. More importantly, as illustrated in Figure 2G, the unique nonequilibrium route reduces the mobility of metal atoms during the formation of the multi-element alloy nanoparticles, traps the metastable state during the phase transition, and effectively suppresses interparticle sintering/coarsening and phase separation/segregation of metal elements. Therefore, NTS is an effective strategy for large-scale nanomanufacturing of high-quality multi-element alloy nanoparticles.

The similar XRD patterns of M-BiSnSb and S-BiSnSb are presented in Figure S1 (Supporting Information). The diffraction peaks of M-BiSnSb can be assigned to a hexagonal phase with the R3_m (166) space group (PDF#35-0517). In addition, the diffraction peaks of M-BiSnSb are slightly lower than those of the above standard card, since Bi and Sb atoms are substituted with Sn atoms. Such a result demonstrates a successful formation of single-phase BiSnSb nanoalloy with the homogeneous mixing of Bi, Sn, and Sb atoms. Furthermore, Rietveld refinement of the SXRD patterns is performed to study the crystal structure of two samples.[30] As shown in **Figure 3A**, the M-BiSnSb crystallizes into a rhombohedral $R\bar{3}m$ structure, with the lattice parameters $a = b = 4.4073$ Å, $c = 11.7094$ Å. For comparison, the M-BiSnSb is further stabilized by tube furnace calcination to remove crystal defects/lattice distortion, which is defined as S-BiSnSb (Figure 3B). It is noted that the lattice parameters ($a = b =$ 4.5327 Å, $c = 11.7903$ Å) of S-BiSnSb have increased significantly. The evident variation of the cell volume further substantiates that the conventional tube furnace annealing with long-term treatment time (≈5 h) and slow cooling rate (≈5 K min^{-1}) can eliminate the crystal defects/lattice distortion of the metastable-state nanoparticles produced by the nonequilibrium synthesis

method. The pair distribution function (PDF) analysis was conducted based on the synchrotron X-ray total scattering data of M-BiSnSb and S-BiSnSb. As illustrated in Figure 3C, the PDF peaks of M-BiSnSb present a positive shift trend after calcination, which can be mainly attributed to the massive elimination of internal lattice distortions/defects. These PDF results are consistent with the SXRD Rietveld refinement calculations.

The morphology and microstructure of the M-BiSnSb were revealed by SEM images in both low and high magnifications (Figure 3D; Figure S2A, Supporting Information). It is observed that the M-BiSnSb nanoparticles supported on the carbon substrate have an ultra-small average particle size of 11.4 nm and high-density dispersion. These morphological features are further demonstrated by the transmission electron microscopy (TEM) images in Figure 3E and Figure S2B (Supporting Information). Figure 3G shows the inverse fast Fourier transform (IFFT) image of the (012) plane from the region of the yellow box in the high-resolution TEM (HRTEM) image of M-BiSnSb (Figure 3F). The inset image of Figure 3G shows the corresponding FFT pattern, where the lattice fringes with an interlayer distance of 3.18 Å are consistent with $d_{(012)}$ of M-BiSnSb. The numerous lattice distortions and crystal defects can be observed inside the M-BiSnSb nanoparticle. The prominent defects consist of many dislocations marked "T". In comparison, TEM images and size distribution of S-BiSnSb obtained by the long-duration annealing show that the S-BiSnSb nanoparticles with an average of 32.8 nm are dispersed across the carbon support (Figure S3A,B, Supporting Information). As shown in Figure S3C,D (Supporting Information), the S-BiSnSb contains almost no dislocations. These results are in good agreement with the SXRD and PDF analyses. The high-angle annular dark-field scanning TEM (HAADF-STEM) and energy-dispersive spectroscopy (EDS) elemental mappings (Figure 3H,I) demonstrate uniform atomic-scale mixing of three constituent elements (Bi, Sn, and Sb) in the M-BiSnSb nanoparticles with no apparent phase separation and element segregation.

The thermogravimetric (TG) analysis in Figure S4 (Supporting Information) shows that the metal content of the M-BiSnSb is ≈66.7 wt%, similar to that of the S-BiSnSb (≈66.3 wt%). X-ray photoelectron spectroscopy (XPS) was carried out to understand the surface characteristics of the M-BiSnSb. The signals of Bi, Sn, Sb, C, N, and O elements are visible in the full spectra (Figure S5A, Supporting Information). According to ICP-MS and XPS quantitative analyses, the molar ratio of Bi, Sn, and Sb in the M-BiSnSb is very close to the molar ratio in the precursor (Bi:Sn:Sb = 1:1:1). Two peaks located at 159.6 and 164.9 eV in the high-resolution Bi 4f spectrum correspond to Bi $4f_{7/2}$ and Bi $4f_{5/2}$, respectively (Figure S5B, Supporting Information). Besides, the binding energy of the Sn 3d high-resolution spectrum in Figure S5C (Supporting Information) is distinguished by the two strong peaks at 487.1 and 495.5 eV, corresponding to Sn $3d_{5/2}$ and Sn $3d_{3/2}$, respectively. The Sb 3d high-resolution spectrum (Figure S5D, Supporting Information) shows two peaks with the binding energy of 531.1 and 540.3 eV, which can be indexed as Sb $3d_{5/2}$ and Sb $3d_{3/2}$, respectively. Because the inevitable oxidation occurred on the surface of the nanoalloy, the binding energy of Bi 4f, Sn 3d, and Sb 3d are higher than those of Bi^0 4f, Sn^0 3d, and Sb^0 3d, which have also been commonly reported in previous studies.[31–34] The high-resolution C 1s spectrum is separated into four peaks at 284.7, 286.3, 288.3, and 290.5 eV, corresponding to the C—C/C=C, C—O/C—N, C=O, and HO—C=O, respectively (Figure S5E, Supporting Information).[35,36] In the high-resolution N 1s spectrum, three peaks corresponding to pyridinic nitrogen (N-6), pyrrolic nitrogen (N-5), and graphitic nitrogen (N-Q) are observed (Figure S5F, Supporting Information).[37,38]

The potassium storage performance of the M-BiSnSb was investigated in the CR2032-type coin half cells. **Figure 4A** presents the cyclic voltammetry (CV) curves for the initial three cycles of the M-BiSnSb anode. During the first negative scan, three wide peaks in the voltage range from 1.0 to 0.02 V appear, which can be attributed to the formation of the solid electrolyte interphase (SEI) cover on the electrode surface, the insertion of K ions into the carbon framework, and the alloying reaction between K and BiSnSb. In the following CV cycles, the reduction peak at 0.02 V should be ascribed to the formation of $K_3BiSnSb$ and the insertion of K^+ into the carbon sheets.[5,39] Moreover, the detailed alloying/dealloying reaction mechanisms will be discussed in **Figure 5**. The inapparent change in the subsequent CV curves implies the high electrochemical reversibility during the K^+ insertion/extraction processes. The galvanostatic charge-discharge (GCD) curves of the M-BiSnSb in Figure 4B show discharge and charge capacities of 594.5 and 350.0 mAh g^{-1}, with an initial Coulombic efficiency (ICE) of 58.9%. The capacity loss during the first cycle is due to the generation of the SEI layer and irreversible potassium intercalation reaction. The nearly superimposed GCD curves at the 50th, 100th, 150th, 200th, 250th, 300th, 350th, and 400th cycles demonstrate excellent cycling stability of the M-BiSnSb anode. The potential of M-BiSnSb as an anode material for KIBs is further confirmed by the rate capability. The rate performance of the M-BiSnSb anode (Figure 4C) shows reversible specific capacities of 410.9, 362.0, 322.5, 278.7, 227.9, and 119.5 mAh g^{-1} at the current density of 0.1, 0.2, 0.5, 1.0, 2.0, and 5.0 A g^{-1}, respectively. Compared with the rate performance of the M-BiSnSb anode, the S-BiSnSb anode shows lower specific capacities and capacity retentions under the same conditions. This comparison suggests that the M-BiSnSb anode has faster potassium intercalation/deintercalation kinetics.

The remarkable cycling stability of M-BiSnSb is shown in Figure 4D, where the specific capacity remains at 343.4 mAh g^{-1} after 400 cycles at a current density of 0.2 A g^{-1}, which is 89.3% of the 10th discharge specific capacity and corresponding to an average capacity decay rate of 0.028% per cycle. Meanwhile, its CE value is over 98% after 8 cycles. In contrast, the S-BiSnSb anode shows a gradual capacity degradation over 400 cycles, resulting in a specific capacity of only 109.1 mAh g^{-1} and a lower capacity retention of 35.5%. Figure 4E shows the long-term cycling stability of M-BiSnSb anodes under a high current density of 1.0 A g^{-1}. It is noted that the M-BiSnSb delivers a reversible specific capacity of 222.2 mAh g^{-1} even after 1000 cycles, with a negligible capacity decay of 0.016% per cycle, corresponding to 83.7% of the 6th specific capacity. However, as the cycle progresses, the S-BiSnSb exhibits unsatisfactory long-term cycling stability, including an unsatisfactory specific capacity of 13.4 mAh g^{-1}, a low capacity retention of 7.94%, and a high capacity decay rate of 0.23% per cycle (Figure S6, Supporting Information) at up to 400 cycles. Significantly, the M-BiSnSb anode is highly competitive with the previously reported Bi/Sn/Sb-based anodes in KIBs (Figure 4F; Table S1, Supporting Information),[40–54] in terms of cycling lifespan and reversible specific capacity. The promising potassium

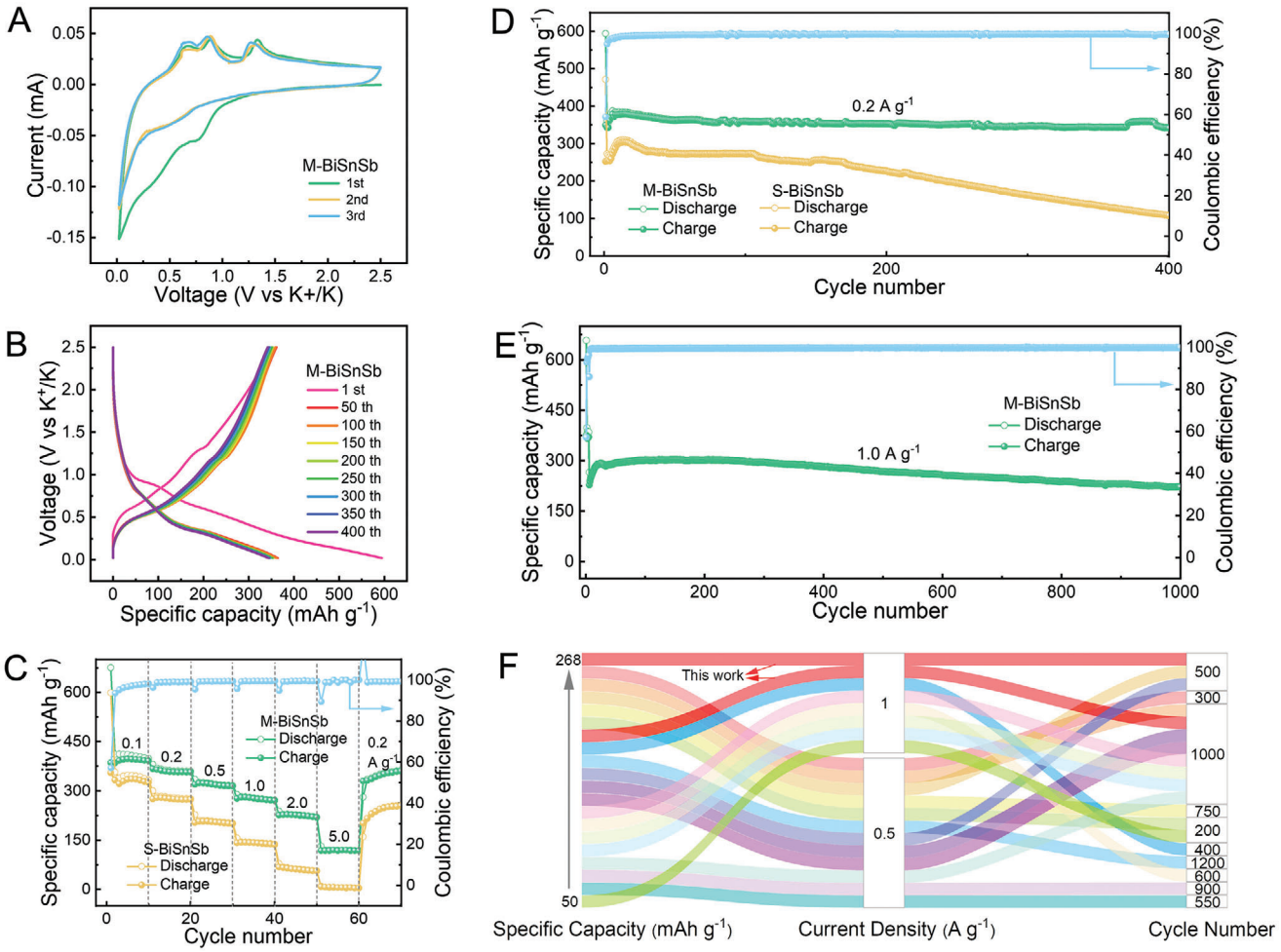

Figure 4. Electrochemical properties of the samples used as anodes for KIBs. A) CV curves of M-BiSnSb in the first three cycles. B) GCD profiles of M-BiSnSb from the 1st to 400th cycles. C) Rate performance of M-BiSnSb and S-BiSnSb. D) Cycling performance of M-BiSnSb and S-BiSnSb at 0.2 A g^{-1}. E) Long-term cycling performance of M-BiSnSb at 1.0 A g^{-1}. F) Comparison in cycling lifespan and specific capacity of M-BiSnSb with other reported Bi/Sn/Sb-based KIBs anodes.

storage performance is related to the unique structural advantages of M-BiSnSb including ultra-fine size, high-density dispersion, and defect-rich metastable structure, which can not only facilitate the potassium intercalation/deintercalation kinetics but also alleviate the mechanical stress induced by volumetric expansion.

To reveal the potassium storage mechanism during the alloying/dealloying of the M-BiSnSb anode, an in situ XRD technique was carried out as shown in Figure 5. During the first discharge process, the characteristic peaks of M-BiSnSb become progressively weaker until they disappear, accompanied by the appearance of the two new peaks. This suggests the alloying reaction of BiSnSb into the KBiSnSb phase. As K^+ is continuously inserted, the KBiSnSb peaks become weaker and the $K_3BiSnSb$ peaks appear. After discharging to 0.02 V, the KBiSnSb peaks fully disappear, proving the complete conversion of the KBiSnSb into the $K_3BiSnSb$. In the subsequent K^+ deintercalation, the $K_3BiSnSb$ phase transforms into the KBiSnSb, and then back to the original BiSnSb, due to the two-step dealloying reaction. Importantly, the structural evolution of BiSnSb during the second K^+ insertion/extraction process is the same as the initial potassiation/depotassiation process, elucidating the highly reversible phase transformation. Notably, it can be found that the diffraction peaks of BiSnSb exhibit minor shifts to lower angles after the 1st cycle compared with the original state. This phenomenon can be ascribed to the slight irreversible alloying/dealloying reaction between K and BiSnSb during the first discharge/charge process, which has been widely observed in previous reports.[3,39,42,43,55] Specifically, a small amount of potassium remained in the alloy structure after the first depotassiation process, thus leading to the increase in the BiSnSb lattice parameters.[56] Since the segregation of Na-Bi, Na-Sn, and Na-Sb phases was not detected in Figure 5A, the alloying/dealloying reactions of BiSnSb proceed possibly through a single alloy phase rather than individual components of Bi, Sn, and Sb. The corresponding alloying/dealloying reaction mechanism of BiSnSb is proposed and summarized as:

$$\text{Potassiation process}: \text{BiSnSb} + K^+ + e^- \rightarrow \text{KBiSnSb} + 2K^+ + 2e^- \rightarrow K_3\text{BiSnSb} \quad (1)$$

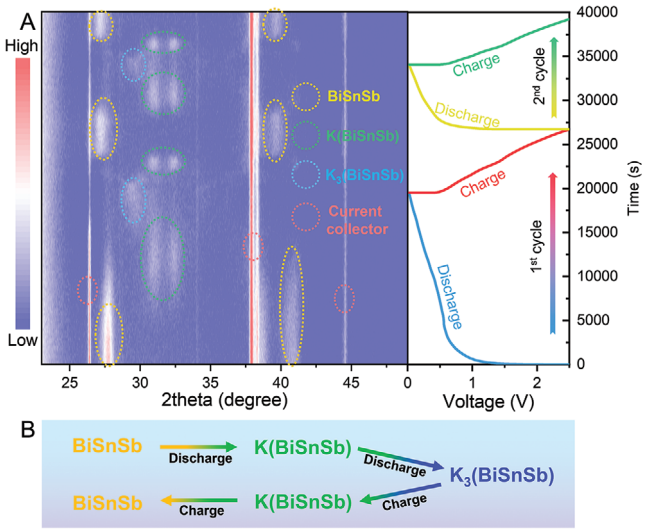

Figure 5. A) In situ XRD patterns of M-BiSnSb and the corresponding GCD curves in the first two cycles. B) Schematic illustration of the alloying/dealloying mechanism of BiSnSb.

$$\text{Depotassiation process}: \quad K_3BiSnSb - 2K^+ - 2e^- \rightarrow KBiSnSb - K^+ - e^- \rightarrow BiSnSb \tag{2}$$

To explore the reason why the M-BiSnSb anode shows outstanding rate capability and cycling stability, the galvanostatic intermittent titration technique (GITT) test was performed. Figure S7B (Supporting Information) exhibits the calculated K^+ diffusion coefficients (D_K) of M-BiSnSb and S-BiSnSb anodes from the corresponding GITT curves (Figure S7A, Supporting Information). The D_K value of M-BiSnSb is higher than that of S-BiSnSb during the charge/discharge processes, indicating that the abundant lattice defects of the M-BiSnSb can provide diffusion pathways for fast ion transport, contributing to the remarkable rate performance.[57,58]

To further validate the structural and morphological stability of the M-BiSnSb anode during the repeated potassiation/depotassiation processes, TEM characterization was performed. The TEM image and the corresponding EDS elemental mapping images of M-BiSnSb after 1000 cycles are shown in Figure S8 (Supporting Information). The original structural integrity of the M-BiSnSb is well maintained, where the ultrasmall nanoparticles uniformly disperse on the carbon substrate without obvious agglomeration, suggesting that the unique nanostructure can facilitate the stress relaxation during repeated K^+ insertion/extraction processes in favor of improved cycling stability. The corresponding EDS elemental mappings further demonstrate the homogeneous distribution of Bi, Sn, Sb, and K in the M-BiSnSb nanocomposite after cycling (Figure S8B, Supporting Information), which is similar to the original M-BiSnSb before cycling.

The K-ion full cell with an M-BiSnSb anode and a PTCDA cathode was assembled to demonstrate the feasibility of the practical application, as demonstrated in Figure S9B (Supporting Information). Before being assembled into a full cell, the PTCDA cathode is tested in half cells, which delivers a reversible capacity of 128.0 mAh g^{-1} at 0.1 A g^{-1} over 50 cycles (Figure S9A, Supporting Information). The rate performance of the M-BiSnSb//PTCDA full cell in Figure S9C (Supporting Information) shows reversible specific capacities of 312.7, 278.4, 240.7, 222.0, 189.5, 151.2, 118.4, 95.6, and 83.4 mAh g^{-1} (calculated based on anode mass) at the current density from 0.2 to 10.0 A g^{-1}, respectively. Besides, the full cell displays a good capacity retention of 221.4 mAh g^{-1} after 100 cycles at 1.0 A g^{-1}, corresponding to 74.3% of its original capacity (Figure S9D, Supporting Information).

To gain a fundamental understanding of the influence of lattice defects on the K diffusion in metastable multi-element nanoalloys, MD simulations were carried out. As shown in Figure S10 (Supporting Information), two different K/BiSnSb diffusion models are built to simulate the diffusion behavior of K atoms into BiSnSb in the absence and presence of a dislocation. **Figure 6A** presents a series of snapshots obtained from the MD simulations showing the K diffusion into the crystalline BiSnSb without dislocation. As the diffusion time gradually increases, it is difficult for K atoms to diffuse into the interior of the BiSnSb alloy (Figure 6B). In contrast to the severe sluggish diffusion of K into the crystalline BiSnSb, when the K slab and the BiSnSb slab with a dislocation come into direct contact with each other, the K diffusion behavior in the metastable BiSnSb is observed along the dislocation core from the interfacial regions (Figure 6C). After continuous diffusion to 100 ps, these K atoms have diffused along the dislocation channel to the depth zone of the BiSnSb alloy (Figure 6D). These simulations demonstrate the internal lattice distortions/defects can provide diffusion channels for the rapid reaction kinetics of the metastable nanoalloy materials in KIBs.

NTS synthesis based on nonequilibrium features (fast heating/quenching rate and short nanomanufacturing duration) can favor homogeneous mixing of multiple elements (Figure S11A, Supporting Information). Therefore, we tried to achieve a collection of multi-element nanoalloys through the NTS route. By tuning metal salt-based precursors, multi-element alloy nanoparticles, such as BiSbPb, BiSnSbZn, BiSnSbPb, and BiSnSbPbZn, were prepared. Figure S12 (Supporting Information) shows the NTS-prepared multi-element alloy nanoparticles have similar diffraction patterns with the corresponding standard cards, accompanied by slight peak shifts, due to the changes in lattice parameters caused by the additional metal elements. Meanwhile, the single-phase structure of these multi-element alloy nanoparticles is elucidated by the absence of obvious phase separation in the XRD patterns. The SEM images, TEM images, and particle size distributions further demonstrate that the obtained nanoparticles have ultrafine average particle sizes (19.7 nm for BiSbPb, 15.4 nm for BiSnSbZn, 14.5 nm for BiSnSbPb, and 21.5 nm for BiSnSbPbZn) with uniform dispersion across the carbon nanosheets. Moreover, EDS elemental mappings (Figure S11B–D, Supporting Information) show the homogeneous distribution of different elements. Consequently, the universal NTS synthetic approach combined with the fast heating/cooling process offers highly efficient and low-cost strategies for the design and synthesis of other multi-element alloy nanomaterials, which provides great potential for the development of energy conversion and storage applications.

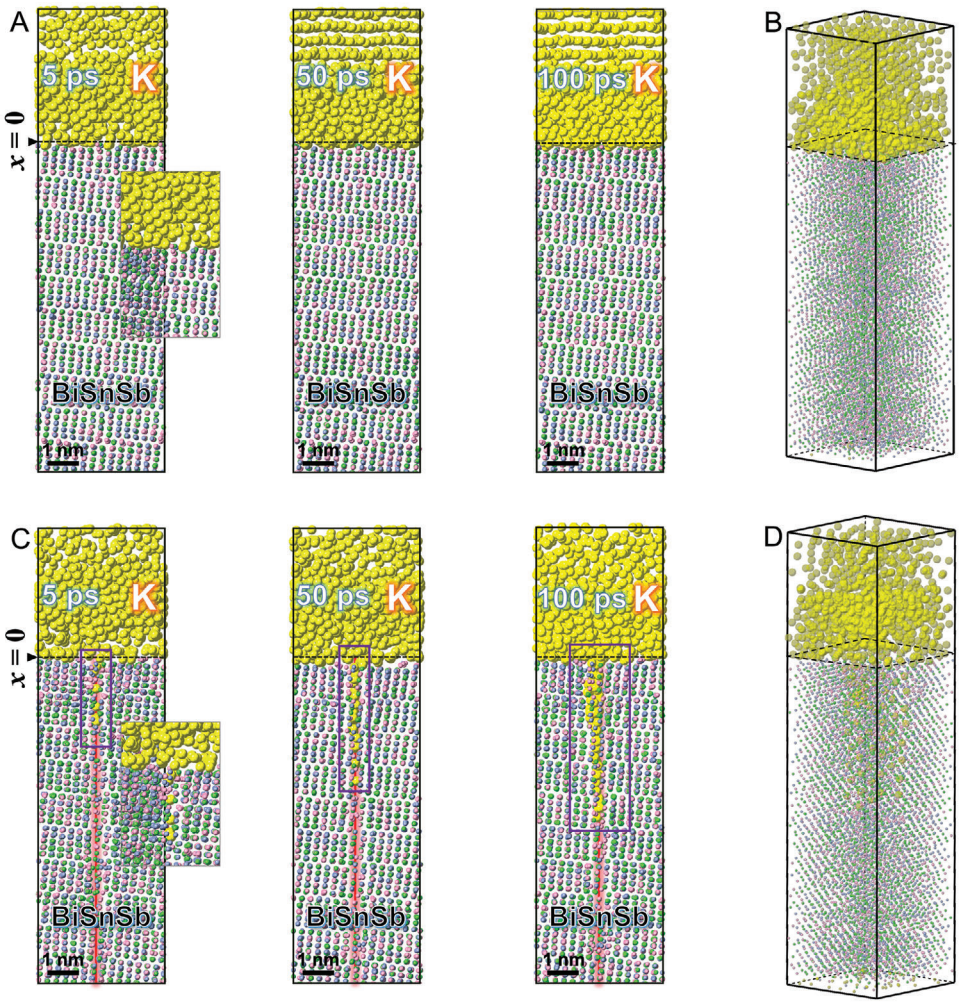

Figure 6. A series of snapshots was obtained from the MD simulations showing the K diffusion into BiSnSb in the A) absence and C) presence of a dislocation. B) 3D view of (A) captured at 100 ps. D) 3D view of (C) captured at 100 ps.

3. Conclusion

In summary, we develop a simple NTS route for the rapid nanomanufacturing of single-phase multi-element alloy nanoparticles with abundant lattice defects, narrow size distribution, and homogeneous dispersion. This method, characterized by the nonequilibrium state and high heating/quenching rate, enables the uniform mixing of different elements and the capture of the metastable state of multi-element nanoalloys while preventing interparticle sintering/coarsening, metal segregation, and phase separation. As a proof-of-concept demonstration, the M-BiSnSb with lattice distortions is synthesized and applied as a KIBs anode. The as-prepared M-BiSnSb anode exhibits superior potassium storage performance (rate capability and long-term cycling stability) compared to the S-BiSnSb anode without defects. In situ high-temperature SXRD shows the structural evaluation of M-BiSnSb during the NTS process. Besides, in situ laboratory XRD clarifies the potassium storage mechanism of BiSnSb $\leftrightarrow$ KBiSnSb $\leftrightarrow K_3$BiSnSb. The MD simulations reveal that the internal lattice distortions/defects are of great significance to the diffusion-accelerating effect in the metastable BiSnSb system, which can offer a diffusion channel for the rapid reaction kinetics in KIBs. This work represents a new strategy for the synthesis of various high-quality multi-element nanoalloys and opens an unlimited space for battery and catalysis applications of new nanomaterials.

Supporting Information

Supporting Information is available from the Wiley Online Library or from the author.

Acknowledgements

This work was financially supported by the fundamental research fund from Shenzhen (JCYJ20220531095214032), and the National Natural Science Foundation of China (grant nos. 92372107 and 52171219). The authors thank the staff of beamline BL13SSW at the Shanghai Synchrotron Radiation Facility and beamline 3W1 at the Beijing Synchrotron Radiation Facility for experiment support.

Conflict of Interest

The authors declare no conflict of interest.

Data Availability Statement

The data that support the findings of this study are available in the supplementary material of this article.

Keywords

mechanism, metastable multi-element nanoalloys, nonequilibrium thermal shock, potassium ion batteries, synchrotron radiation diffraction

Received: July 15, 2024
Revised: August 30, 2024
Published online:

[1] X. Min, J. Xiao, M. Fang, W. Wang, Y. Zhao, Y. Liu, A. M. Abdelkader, K. Xi, R. V. Kumar, Z. Huang, *Energy Environ. Sci.* **2021**, *14*, 2186.
[2] L. Fan, R. Ma, Q. Zhang, X. Jia, B. Lu, *Angew. Chem., Int. Ed.* **2019**, *58*, 10500.
[3] K.-T. Chen, H.-Y. Tuan, *ACS Nano* **2020**, *14*, 11648.
[4] J. Wang, L. Fan, Z. Liu, S. Chen, Q. Zhang, L. Wang, H. Yang, X. Yu, B. Lu, *ACS Nano* **2019**, *13*, 3703.
[5] L. Yang, L. Guo, D. Yan, Y. Wang, T. Shen, D.-S. Li, M. E. Pam, Y. Shi, H. Y. Yang, *ACS Nano* **2023**, *17*, 6754.
[6] J. Wang, Z. Liu, J. Zhou, K. Han, B. Lu, *ACS Mater. Lett.* **2021**, *3*, 1572.
[7] Z. Xiao, X. Wang, J. Meng, H. Wang, Y. Zhao, L. Mai, *Mater. Today* **2022**, *56*, 114.
[8] X. Zheng, X. Gao, R. A. Vila, Y. Jiang, J. Wang, R. Xu, R. Zhang, X. Xiao, P. Zhang, L. C. Greenburg, Y. Yang, H. L. Xin, X. Zheng, Y. Cui, *Nat. Nanotechnol.* **2023**, *18*, 153.
[9] S. Moniri, Y. Yang, J. Ding, Y. Yuan, J. Zhou, L. Yang, F. Zhu, Y. Liao, Y. Yao, L. Hu, P. Ercius, J. Miao, *Nature* **2023**, *624*, 564.
[10] S. Weng, S. Wu, Z. Liu, G. Yang, X. Liu, X. Zhang, C. Zhang, Q. Liu, Y. Huang, Y. Li, M. N. Ates, D. Su, L. Gu, H. Li, L. Chen, R. Xiao, Z. Wang, X. Wang, *Carbon Energy* **2023**, *5*, e224.
[11] J. Luo, J. Zhang, Z. Guo, Z. Liu, S. Dou, W.-D. Liu, Y. Chen, W. Hu, *Nano Res.* **2023**, *16*, 4240.
[12] A. Sarkar, Q. Wang, A. Schiele, M. R. Chellali, S. S. Bhattacharya, D. Wang, T. Brezesinski, H. Hahn, L. Velasco, B. Breitung, *Adv. Mater.* **2019**, *31*, 1806236.
[13] S. Schweidler, M. Botros, F. Strauss, Q. Wang, Y. Ma, L. Velasco, G. C. Marques, A. Sarkar, C. Kuebel, H. Hahn, J. Aghassi-Hagmann, T. Brezesinski, B. Breitung, *Nat. Rev. Mater.* **2024**, *9*, 266.
[14] L. Wu, H. Fu, S. Li, J. Zhu, J. Zhou, A. M. Rao, L. Cha, K. Guo, S. Wen, B. Lu, *Nat. Commun.* **2023**, *14*, 644.
[15] Z. Yi, N. Lin, T. Li, Y. Han, Y. Li, Y. Qian, *Nano Res.* **2019**, *12*, 1824.
[16] Y. Yao, Q. Dong, A. Brozena, J. Luo, J. Miao, M. Chi, C. Wang, I. G. Kevrekidis, Z. J. Ren, J. Greeley, G. Wang, A. Anapolsky, L. Hu, *Science* **2022**, *376*, eabn3103.
[17] Z. Lun, B. Ouyang, D.-H. Kwon, Y. Ha, E. E. Foley, T.-Y. Huang, Z. Cai, H. Kim, M. Balasubramanian, Y. Sun, J. Huang, Y. Tian, H. Kim, B. D. McCloskey, W. Yang, R. J. Clement, H. Ji, G. Ceder, *Nat. Mater.* **2021**, *20*, 214.
[18] Y. Yao, Z. Huang, P. Xie, S. D. Lacey, R. J. Jacob, H. Xie, F. Chen, A. Nie, T. Pu, M. Rehwoldt, D. Yu, M. R. Zachariah, C. Wang, R. Shahbazian-Yassar, J. Li, L. Hu, *Science* **2018**, *359*, 1489.
[19] J.-H. Cha, S.-H. Cho, D.-H. Kim, D. Jeon, S. Park, J.-W. Jung, I.-D. Kim, S.-Y. Choi, *Adv. Mater.* **2023**, *35*, 2305222.
[20] M. Cui, C. Yang, S. Hwang, M. Yang, S. Overa, Q. Dong, Y. Yao, A. H. Brozena, D. A. Cullen, M. Chi, T. F. Blum, D. Morris, Z. Finfrock, X. Wang, P. Zhang, V. G. Goncharov, X. Guo, J. Luo, Y. Mo, F. Jiao, L. Hu, *Sci. Adv.* **2022**, *8*, eabm4322.
[21] J. Park, M. K. Kabiraz, H. Kwon, S. Park, H. Baik, S.-I. Choi, K. Lee, *ACS Nano* **2017**, *11*, 10844.
[22] Y. Yao, Z. Liu, P. Xie, Z. Huang, T. Li, D. Morris, Z. Finfrock, J. Zhou, M. Jiao, J. Gao, Y. Mao, J. Miao, P. Zhang, R. Shahbazian-Yassar, C. Wang, G. Wang, L. Hu, *Sci. Adv.* **2020**, *6*, eaaz0510.
[23] Y. Yao, Z. Huang, T. Li, H. Wang, Y. Liu, H. S. Stein, Y. Mao, J. Gao, M. Jiao, Q. Dong, J. Dai, P. Xie, H. Xie, S. D. Lacey, I. Takeuchi, J. M. Gregoire, R. Jiang, C. Wang, A. D. Taylor, R. Shahbazian-Yassar, L. Hu, *Proc. Natl. Acad. Sci. USA* **2020**, *117*, 6316.
[24] D. Morris, Y. Yao, Y. Z. Finfrock, Z. Huang, R. Shahbazian-Yassar, L. Hu, P. Zhang, *Cell Rep. Phys. Sci.* **2021**, *2*, 100641.
[25] B. Wang, C. Wang, X. Yu, Y. Cao, L. Gao, C. Wu, Y. Yao, Z. Lin, Z. Zou, *Nat. Synth.* **2022**, *1*, 138.
[26] D. Liu, Z. Shadike, R. Lin, K. Qian, H. Li, K. Li, S. Wang, Q. Yu, M. Liu, S. Ganapathy, X. Qin, Q.-H. Yang, M. Wagemaker, F. Kang, X.-Q. Yang, B. Li, *Adv. Mater.* **2019**, *31*, 1806620.
[27] X. Liu, Y. Tong, Y. Wu, J. Zheng, Y. Sun, H. Li, *Small Methods* **2021**, *5*, 2101130.
[28] Z. Huang, Y. Yao, Z. Pang, Y. Yuan, T. Li, K. He, X. Hu, J. Cheng, W. Yao, Y. Liu, A. Nie, S. Sharifi-Asl, M. Cheng, B. Song, K. Amine, J. Lu, T. Li, L. Hu, R. Shahbazian-Yassar, *Nat. Commun.* **2020**, *11*, 6373.
[29] C. Yang, B. H. Ko, S. Hwang, Z. Liu, Y. Yao, W. Luc, M. Cui, A. S. Malkani, T. Li, X. Wang, J. Dai, B. Xu, G. Wang, D. Su, F. Jiao, L. Hu, *Sci. Adv.* **2020**, *6*, eaaz6844.
[30] B. H. Toby, R. B. Von Dreele, *J. Appl. Crystallogr.* **2013**, *46*, 544.
[31] L. Wang, B. Zhang, B. Wang, S. Zeng, M. Zhao, X. Sun, Y. Zhai, L. Xu, *Angew. Chem., Int. Ed.* **2021**, *60*, 15381.
[32] K. Huang, Z. Xing, L. Wang, X. Wu, W. Zhao, X. Qi, H. Wang, Z. Ju, *J. Mater. Chem. A* **2018**, *6*, 434.
[33] H. Huang, J. Wang, X. Yang, R. Hu, J. Liu, L. Zhang, M. Zhu, *Angew. Chem., Int. Ed.* **2020**, *59*, 14504.
[34] Y. Liang, N. Song, Z. Zhang, W. Chen, J. Feng, B. Xi, S. Xiong, *Adv. Mater.* **2022**, *34*, 2202673.
[35] F. Xie, Y. Niu, Q. Zhang, Z. Guo, Z. Hu, Q. Zhou, Z. Xu, Y. Li, R. Yan, Y. Lu, M.-M. Titirici, Y.-S. Hu, *Angew. Chem., Int. Ed.* **2022**, *61*, 202116394.
[36] S. Dou, J. Xu, D. Zhang, W. Liu, C. Zeng, J. Zhang, Z. Liu, H. Wang, Y. Liu, Y. Wang, Y. He, W.-D. Liu, W. Gan, Y. Chen, Q. Yuan, *Angew. Chem., Int. Ed.* **2023**, *62*, 202303600.
[37] Y. Chen, B. Xi, M. Huang, L. Shi, S. Huang, N. Guo, D. Li, Z. Ju, S. Xiong, *Adv. Mater.* **2022**, *34*, 2108621.
[38] J. Yin, J. Jin, C. Chen, Y. Lei, Z. Tian, Y. Wang, Z. Zhao, A.-H. Emwas, Y. Zhu, Y. Han, U. Schwingenschloegl, W. Zhang, H. N. Alshareef, *Angew. Chem., Int. Ed.* **2023**, *62*, 202301396.
[39] X. Liu, X. Wang, Y. Zhou, B. Wang, L. Zhao, H. Zheng, J. Wang, J. Liu, J. Liu, Y. Li, *Adv. Mater.* **2024**, *36*, 2308447.
[40] C. Huang, A. Xu, G. Li, H. Sun, S. Wu, Z. Xu, Y. Yan, *Small* **2021**, *17*, 2100685.
[41] C.-H. Chang, K.-T. Chen, Y.-Y. Hsieh, C.-B. Chang, H.-Y. Tuan, *ACS Nano* **2022**, *16*, 1486.
[42] J. Liu, D. Zhang, J. Cui, P. Li, X. Xu, Z. Liu, J. Liu, C. Peng, D. Xue, M. Zhu, J. Liu, *Small* **2023**, *19*, 2301444.
[43] K.-T. Chen, Y.-C. Yang, L.-M. Lyu, M.-Y. Lu, H.-Y. Tuan, *Nano Energy* **2021**, *88*, 106233.
[44] X. Liu, J. Zhu, X. Wang, L. Yue, W. Wang, B. Wang, D. Shen, Y. Li, *Adv. Funct. Mater.* **2023**, *33*, 2209388.
[45] Q. Wu, B. Chen, H. Xie, X. Bai, M. Liang, Z. Wu, X. Jin, C. He, N. Zhao, *Chem. Eng. J.* **2022**, *430*, 132906.
[46] X. Tian, P. Zhang, Y. Liao, R. A. Soomro, B. Xu, *Small Methods* **2023**, *7*, 2201525.

[47] J. Li, G. Wang, L. Yu, J. Gao, Y. Li, S. Zeng, G. Zhang, *ACS Appl. Mater. Interfaces* **2021**, *13*, 13139.
[48] W.-C. Lin, Y.-C. Yang, H.-Y. Tuan, *Energy Storage Mater.* **2022**, *51*, 38.
[49] Z. Li, J. Wen, Y. Cai, F. Lv, X. Zeng, Q. Liu, T. Masese, C. Zhang, X. Yang, Y. Ma, H. Zhang, Z.-D. Huang, *Adv. Funct. Mater.* **2023**, *33*, 2300582.
[50] Q. Luo, J. Wen, G. Liu, Z. Ye, Q. Wang, L. Liu, X. Yang, *J. Power Sources* **2022**, *545*, 231917.
[51] C. Li, A. T. Bi, H. L. Chen, Y. R. Pei, M. Zhao, C. C. Yang, Q. Jiang, *J. Mater. Chem. A* **2021**, *9*, 5740.
[52] P. Zhang, Y. Wei, S. Zhou, R. A. Soomro, M. Jiang, B. Xu, *J. Colloid Interface Sci.* **2023**, *630*, 365.
[53] J. Zhang, G. Kim, M. Park, J. Zhang, S. Lee, Y. Cui, K. Zhang, F. Zou, Y.-M. Kang, *Adv. Energy Mater.* **2022**, *12*, 2202446.
[54] T. Yuan, J. Yan, Q. Zhang, Y. Su, S. Xie, B. Lu, J. Huang, X. Ouyang, *ACS Nano* **2023**, *17*, 10462.
[55] P. Xiong, J. Wu, M. Zhou, Y. Xu, *ACS Nano* **2020**, *14*, 1018.
[56] X.-D. He, J.-Y. Liao, S. Wang, J.-R. Wang, Z.-H. Liu, X. Ding, Q. Hu, Z.-Y. Wen, C.-H. Chen, *J. Mater. Chem. A* **2019**, *7*, 27041.
[57] Y. Zhang, L. Tao, C. Xie, D. Wang, Y. Zou, R. Chen, Y. Wang, C. Jia, S. Wang, *Adv. Mater.* **2020**, *32*, 1905923.
[58] J.-H. Kim, Y.-H. Lee, J.-H. Park, B.-J. Lee, Y.-W. Byeon, J.-C. Lee, *Small* **2022**, *18*, 2104944.